Applied Catalysis B: Environmental 138–139 (2013) 427–433

Contents lists available at SciVerse ScienceDirect

Applied Catalysis B: Environmental

journal homepage: www.elsevier.com/locate/apcatb

Hierarchically porous silicon with significantly improved photocatalytic oxidation capability for phenol degradation

Jingyang Su [a], Hongtao Yu [a], Xie Quan [a,*], Shuo Chen [a], Hua Wang [b]

[a] Key Laboratory of Industrial Ecology and Environment Engineering (Ministry of Education), School of Environmental Science and Technology, Dalian University of Technology, Dalian 116024, China
[b] College of Fisheries and Life Science, Dalian Ocean University, Dalian 116023, China

ARTICLE INFO

Article history:
Received 14 September 2012
Received in revised form 11 February 2013
Accepted 1 March 2013
Available online 18 March 2013

Keywords:
Porous silicon
Quantum confinement effect
Photocatalytic oxidation
Stability

ABSTRACT

In this work, hierarchically porous silicon was fabricated through electro-assisted chemical etching using a silicon wafer as a substrate. Pores with an average diameter of ca. 1200 nm (macropores) were observed and a large number of nanopores with a diameter of less than 5 nm were uniformly distributed over the surface of the macropore, forming the hierarchically porous silicon with nanopores in macropores structure (NP-MPSi). UV–vis diffuse reflection measurements indicated that NP-MPSi has a bandgap of 2.12 eV, which is 1.0 eV higher than that of the original silicon wafer because of the quantum confinement effect caused by the nanopores. Mott–Schottky experiments further demonstrated that the increase in bandgap of NP-MPSi arises from a positive shift of the valence band potential, which improves its capability for photocatalytic oxidation. NP-MPSi exhibited higher photoelectrochemical stability than macroporous silicon (MPSi), a comparison sample lacking nanopores. Using phenol as an example, photocatalytic experiments under irradiation with a Xe lamp demonstrated that the kinetic constants of phenol degradation and total organic carbon removal using NP-MPSi were nearly 3.5 and 8.0 times larger, respectively, than those using MPSi. This unique porous silicon material is therefore an attractive photocatalyst for environmental applications.

1. Introduction

In recent years, semiconducting nanomaterials with narrow bandgap have attracted great attention because of their potential as visible light photocatalysts for environmental remediation and solar energy conversion [1–4]. To date, many research groups have developed different kinds of photocatalysts that are active under visible light such as doped or sensitized TiO_2 [5,6], $BiVO_4$ [7], $BaBiO_3$ [8], Bi_2FeO_3 [9], $CdInS_4$ [10], and $InNbO_4$ [11].

Compared with the above mentioned visible-light-response photocatalysts, silicon (Si) has been proposed as an alternative high performance photocatalyst with a wide spectral response because of the following advantages: (1) Si can absorb UV, visible and even infrared light, which greatly increases the percentage of light energy used, (2) the conduction band (CB) energy level of Si is −0.5 eV (pH = 0), which is more negative than most reported visible light photocatalysts, and thus photogenerated electrons have high reductive ability that benefits hydrogen production or pollutant reduction, (3) as the most widely used material in the electronics industry, Si has an across-the-board knowledge base and manufacturing infrastructure, allowing feasible control of antireflective surfaces to realize highly efficient light harvesting, (4) Si is one of the most abundant elements and its processing technology is mature, so Si is potentially a cost-effective material for use as a photocatalyst.

Despite Si materials possessing the advantages mentioned above, their passivation in aqueous solution [12,13] usually limits their application as photocatalysts in environmental remediation and solar energy conversion. Some researchers have attempted to improve the stability of Si in aqueous solution. A general approach is to cover a silicon surface with a protection layer with a thickness of several nanometers, such as wide-bandgap semiconductors [14], graphene [15], noble metals [16] and polymer films [17]. However, these protection layers usually block absorption of incident light by the photocatalyst, and the layer may peel off from silicon surface during operation. Meanwhile, the valence band (VB) energy level of Si is about 0.6 eV (pH = 0), which is lower than the oxidation potential of most environmental pollutants [18]. The poor oxidation ability of pristine Si makes it unsuitable for photocatalytic oxidation of most pollutants. Although there are some reports related to application of silicon nanowires in photocatalysis, most of them use the reduction capability of silicon instead of poor oxidation ability

* Corresponding author at: School of Environmental Science and Technology, Dalian University of Technology, Linggong Road 2, Dalian 116024, China. Tel.: +86 411 84706140; fax: +86 411 84706263.
E-mail address: quanxie@dlut.edu.cn (X. Quan).

0926-3373/$ – see front matter © 2013 Elsevier B.V. All rights reserved.
http://dx.doi.org/10.1016/j.apcatb.2013.03.014

[19–22]. Thus, enhancing the oxidation capability of silicon materials to meet the requirements of practical applications remains a challenge.

In this work, a hierarchically porous silicon material that is composed of a macroporous infrastructure and nanoporous surface (denoted NP-MPSi) is designed. Nanopores promote the quantum confinement effect, which should improve the photocatalytic oxidation ability and stability of silicon materials. The photocatalytic ability of the hierarchically porous silicon materials under visible light irradiation is evaluated using phenol as a target. The relative photocatalytic mechanisms extrapolated from the experimental results are also discussed.

2. Experimental

2.1. Preparation of NP-MPSi

NP-MPSi samples were prepared by anodic etching of a Si wafer (n-type, (100) orientation, 2–8 Ω cm resistivity, 525 μm thick) in 49% HF/ethanol solution (v:v = 1:1) under irradiation with a Xe lamp (light intensity of 100 mW cm^{-2}) at a current density of 50 mA cm^{-2} for 15 min using a Pt electrode as the counter electrode. After etching, the samples were rinsed with ethanol and then dried under a stream of nitrogen gas. For comparison, a sample containing only macropores (MPSi) was prepared under the same conditions as NP-MPSi except that the volume ratio of the 49% HF/ethanol solution was 1:4 and the solution was not illuminated with a Xe lamp.

2.2. Characterizations of structural and optical properties

The morphologies and crystallographic structures of the samples were characterized by field emission scanning electron microscopy (FE-SEM, S-4800, Hitachi) and transmission electron microscopy (TEM, FEI-Tecnai G^2 20), respectively. The optical absorption and reflection of samples were recorded on a Shimadzu UV-2450 UV/Vis spectrophotometer with an integrating sphere. Pore size distributions were measured using an automated surface area and pore size analyzer (Quantachrome Quadrasorb SI4).

2.3. Evaluation of photocatalytic activity of NP-MPSi

Electrochemical measurements were performed in a three-electrode cell using a CHI 660B electrochemical station (CH Instruments, Shanghai Chenhua, China). A silicon sample (NP-MPSi, MPSi, or Si wafer), a platinum foil and saturated calomel electrode were used as the working electrode, counter electrode and reference electrode, respectively.

Photocatalytic experiments were performed in a quartz reactor with a volume of 50 mL under magnetic stirring and irradiation with a Xe lamp (light intensity of 100 mW cm^{-2}). The initial concentration of phenol was 5 mg L^{-1} and the volume of phenol solution was 10 mL. During the photocatalytic reaction, each photocatalytic material (NP-MPSi, MPSi or Si wafer) was placed vertically in the solution, and their active areas (5 cm^2) were irradiated with incident light. The concentration of phenol was analyzed by high performance liquid chromatography (HPLC, Waters 2695, Photodiode Array Detector 2996) using a Kromasil ODS column (250 mm × 4.6 mm × 5 μm) at a detector wavelength of 280 nm. The mobile phase was methanol:water = 55:45 (v:v) with a flow rate of 0.5 mL min^{-1}. Total organic carbon (TOC) was measured using a TOC analyzer (TOC-V_{CPH}, Shimadzu, Japan).

3. Results and discussion

3.1. Morphology and pore size distribution

The typical features of the NP-MPSi samples are shown in Fig. 1. A cross-sectional SEM image of NP-MPSi is presented in Fig. 1A. Macropores with an average diameter of ca. 1200 nm were uniformly distributed over the whole Si wafer (inset in Fig. 1A), and each was positioned perpendicular to the Si substrate with little side branching. As shown in Fig. 1B, a similar microstructure was observed for MPSi. To further characterize the structure of the macropores, the samples were observed by TEM. Interestingly, numerous nanopores were clearly observed on the surface of NP-MPSi (Fig. 1C), while no nanopores were observed in MPSi (Fig. 1D).

To obtain further information about the porous structures in NP-MPSi, the pore size distributions of the samples were determined, as shown in Fig. 2. About 80% of the pore volume of NP-MPSi was found in nanopores with diameters less than 20 nm (Fig. 2A). Furthermore, the proportion of pores with a diameter of less than 5 nm is considerable (about 60%, inset in Fig. 2A). For MPSi, no pores with diameters less than 5 nm were observed (Fig. 2B). Delerue et al. summarized accurate calculations of the quantum confinement effect for nano-Si materials [23], and revealed that the threshold for quantum confinement effect in nano-Si including nanocrystals, nanowires and nanopores is less than 5 nm, and that the bandgap energy significantly increases as the size of a nano-Si material decreases [24–27]. Therefore, the quantum confinement effect could occur in NP-MPSi because of the presence of nanopores with a diameter of less than 5 nm, and subsequently its bandgap is wider than that of MPSi.

3.2. Energy bands

Optical absorption measurements obtained for NP-MPSi and MPSi are presented in Fig. 3A. Obviously, the absorption intensity of NP-MPSi is higher than that of MPSi in the measured wavelength range. Using the results of UV–vis diffuse reflection measurements, bandgap energy can be estimated from a plot of $(\alpha h\nu)^{1/2}$ versus photon energy ($h\nu$) [28]. The intercept of the tangent to the plot will give a good approximation of the bandgap energy for indirect bandgap materials (e.g., Si). According to the quantum confinement effect, when the size of nanopore is small enough, its band gap energy will increase with its diameter decreasing. NP-MPSi is with innumerable nanopores in a range from several nanometers to tens of nanometers (Fig. 2A), and sequentially, its band gap will be mixed with multiple gaps. Therefore, it is impossible to position the band gap with only one tangent. However, for convenience in the following discussion, a typical value, 2.12 eV, in the range of these multiple gaps was selected and the corresponding tangent was shown in Fig. 3B. Analogously, the energy gap of MPSi was estimated as 1.12 eV. Compared with the energy gap of the pristine Si wafer (1.12 eV) or MPSi, the value of NP-MPSi is 1.0 eV higher, indicating its band gap widened due to quantum confinement effect.

Electrochemical experiments were performed to explore the bandgap broadening of NP-MPSi. Generally, if the pH of a solution is 0, the potential of the CB approximately equals the flat band potential (E_{fb}). E_{fb} can be obtained by extrapolating the potential of the linear region to intercept the potential axis at $1/C^2 = 0$ (C is the space charge capacity). The Mott–Schottky analysis was carried out by conducting a standard electrochemical impedance spectroscopy at 3000 Hz in H_2SO_4 solution (pH = 0) by scanning the potential from positive to negative direction in steps of 20 mV s^{-1} under xenon lamp illumination (light intensity was 100 mW cm^{-2}). Fig. 3C shows the Mott–Schottky plots for NP-MPSi and MPSi. For NP-MPSi, E_{fb} was calculated to be −0.55 eV. Therefore, the CB potential of NP-MPSi was about −0.55 eV, and the VB potential of NP-MPSi can

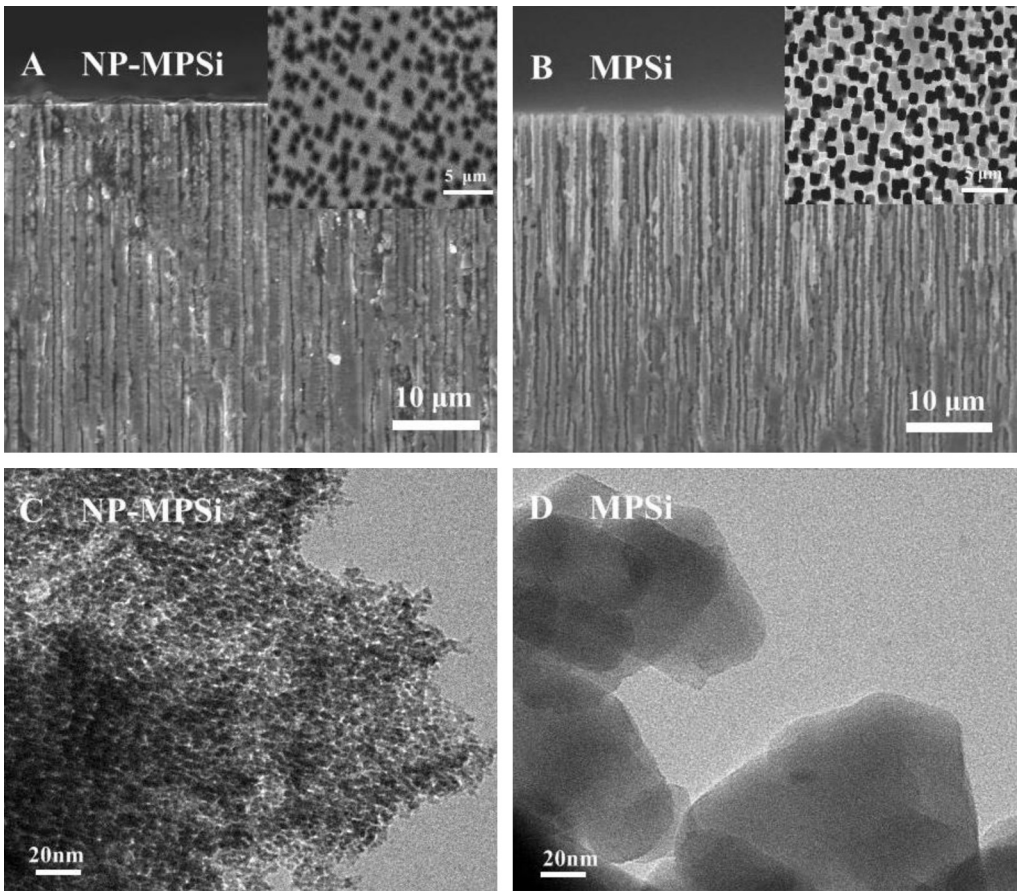

Fig. 1. Profile and top-view SEM images of NP-MPSi (A and its inset) and MPSi (B and its inset), TEM images of NP-MPSi (C) and MPSi (D).

be calculated to be 1.57 eV by subtracting the absolute value of the CB potential from the bandgap energy of NP-MPSi (2.12 eV), which is higher than the oxidation potential of water (1.23 eV) and most of pollutants (e.g., phenol, about 1.0 eV [29]). The above results indicate that NP-MPSi possesses a sufficiently high photocatalytic oxidation ability to decompose water and pollutants.

3.3. Photocatalytic oxidation capability

The photocatalytic activity of NP-MPSi was evaluated by its ability to photocatalytically degrade phenol. As shown in Fig. 4A, nearly 10% of the phenol was removed in the dark in the presence of NP-MPSi after 5 h of reaction, which was ascribed to the adsorption of phenol on NP-MPSi. For direct photolysis under Xe lamp irradiation without NP-MPSi, about 53% of the phenol was removed. The removal efficiency of phenol using MPSi as a photocatalyst was similar to that achieved by direct photolysis. In contrast, more than 95% of the phenol was removed after 5 h of photocatalytic reaction in the presence of NP-MPSi, indicating a significantly improved photocatalytic oxidation capability compared with MPSi. The corresponding rate constants (pseudo first order kinetics) of phenol degradation using NP-MPSi and MPSi were -0.49 and $-0.14\,h^{-1}$, respectively. The degradation rate of phenol using NP-MPSi was almost 2.5 times higher than that using MPSi. Fig. 4B shows the TOC removal efficiency of NP-MPSi and MPSi. The TOC removal efficiency of phenol increased with reaction time and reached 45% for NP-MPSi after

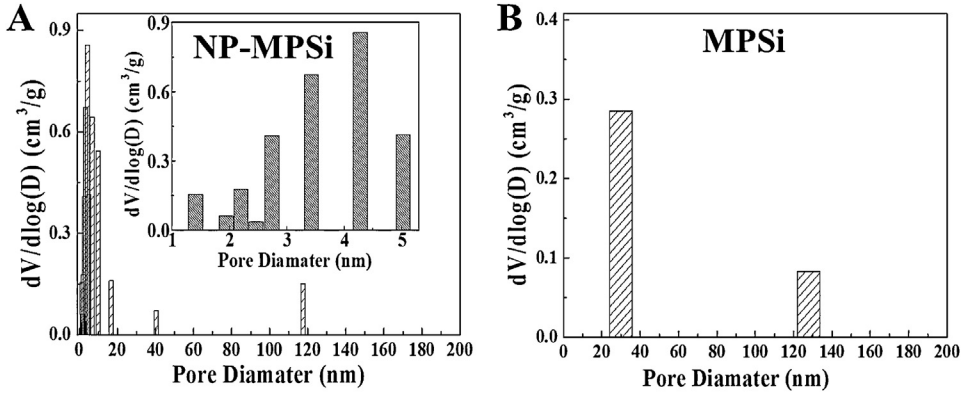

Fig. 2. Pore size distributions of (A) NP-MPSi and (B) MPSi.

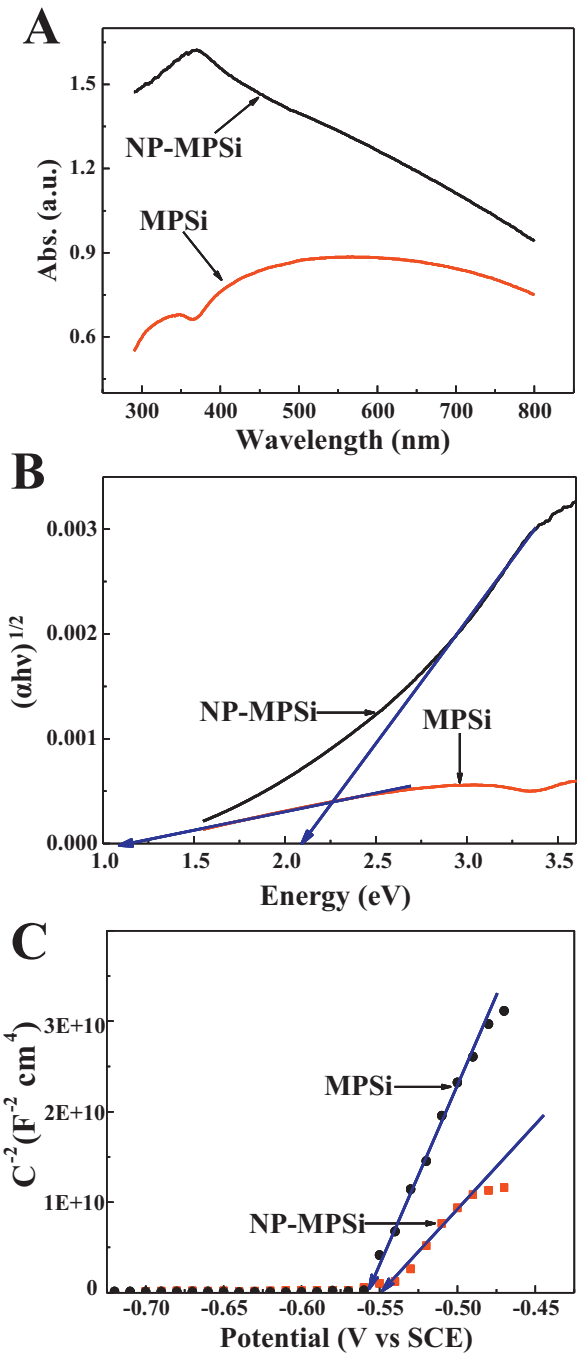

Fig. 3. (A) Absorption spectra of NP-MPSi and MPSi, (B) Plots of $(\alpha h\nu)^{1/2}$ versus photon energy ($h\nu$) for NP-MPSi and MPSi, (C) Mott–Schottky plots showing the flat band potential of NP-MPSi and MPSi in H_2SO_4 (pH = 0) under irradiation (light intensity of 100 mW cm^{-2}).

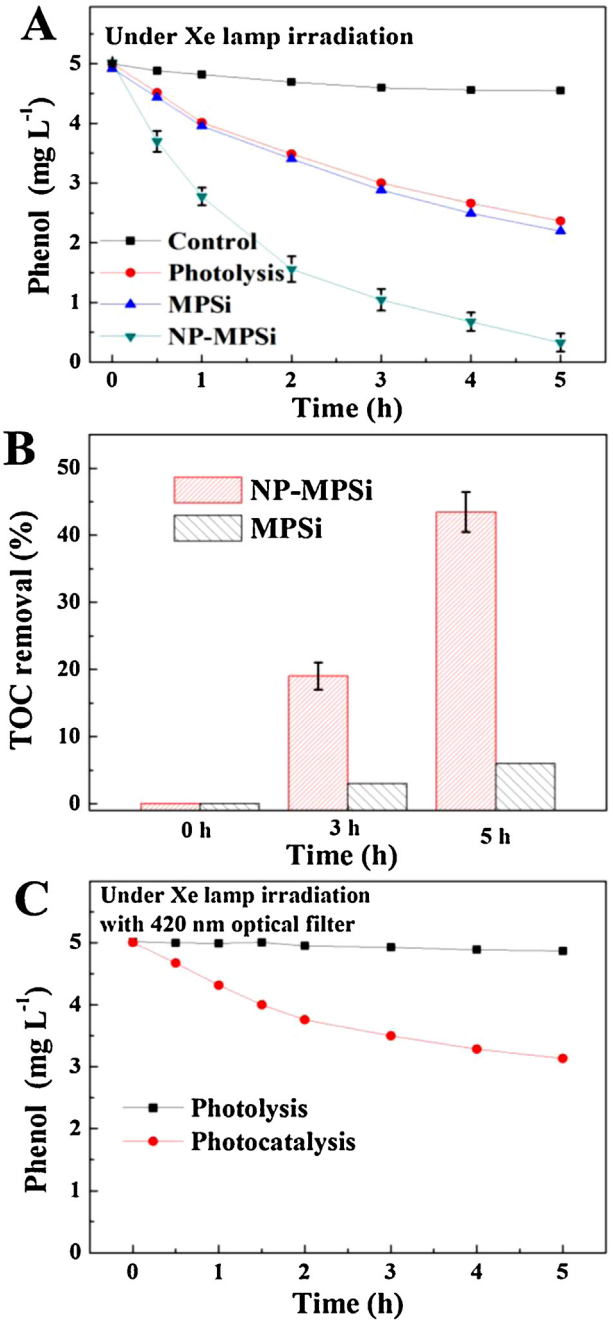

Fig. 4. (A) Removal of phenol by various processes, (B) TOC removal during phenol degradation and (C) removal of phenol under visible light by NP-MPSi (light intensity of 100 mW cm^{-2}).

5 h of reaction, which is nearly 8.0 times that observed for MPSi, demonstrating a better mineralization ability using NP-MPSi as a photocatalyst than MPSi.

NP-MPSi was also evaluated as a visible light photocatalyst using a Xe lamp equipped with a 420 nm optical filter to remove UV light (Fig. 4C). No phenol was removed during direct photolysis, whereas 37% of phenol was removed after 5 h of reaction in the presence of NP-MPSi. We believe the removal efficiency could be improved further when the preparation and photocatalysis conditions are optimized. This result demonstrates that photocatalytic oxidation by NP-MPSi can be induced by visible light, which makes it very attractive for use as a solar energy photocatalyst.

3.4. Stability in aqueous solution

The photoelectrochemical stability of NP-MPSi was also evaluated by measuring 20 cyclic voltammograms (CVs). Fig. 5A shows CVs obtained using different photoanodes including NP-MPSi, MPSi and a Si wafer in 0.5 M H_2SO_4 under Xe lamp irradiation. It can be observed from Fig. 5A that photocurrent of the Si wafer was obviously lower than that of MPSi or NP-MPSi. For MPSi, the initial photocurrent was a little more than 6 mA cm^{-2} (at 1.5 V vs. SCE), and then it decreased sharply to 1.8 mA cm^{-2} after 20 cycles. In contrast, the photocurrent of NP-MPSi kept stable and remained

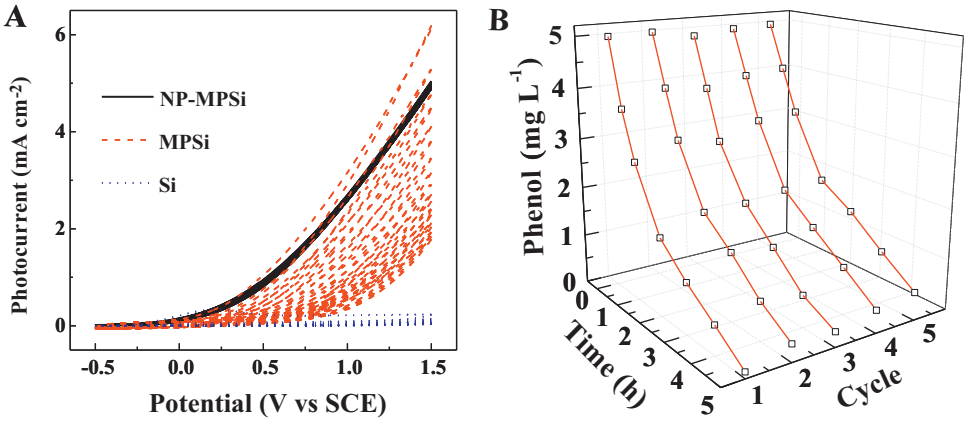

Fig. 5. (A) CVs of NP-MPSi, MPSi and a Si wafer in 0.5 M H_2SO_4 under Xe lamp irradiation and (B) five consecutive cycling experiments using the same NP-MPSi (light intensity of 100 mW cm^{-2}).

high level (about 5 mA cm^{-2} at 1.5 V (vs. SCE)) even after 20 cycles, which was nearly 3 times as great as that of MPSi.

It is easy to understand the attenuation of the photocurrent on MPSi. According to the work of Zhang on Si and its oxide [30], a silica oxidation layer may form on the surface of bulk silicon (such as Si or MPSi) in aqueous solution during electrochemical cycling, which could block electron transfer between the electrolyte and Si materials, resulting in attenuation of the photocurrent. As regards the good stability of NP-MPSi, we deem that it is caused by nanopores on the macropore surface, because the existence of these nanopores is the only difference between NP-MPSi and MPSi. According to the work of Wilson et al. [27,31], once the size of Si materials be less than several nanometers, the quantum confinement effect would happened, and under the action of the quantum confinement effect, some dangling bonds of Si would be saturated by hydrogen atoms instead of being terminated fully by oxygen. As a result, the passivation of these nano-size Si materials would be reduced. For NP-MPSi of this work, there are nanopores less than 5 nm throughout the surface, whose sizes are small enough for causing quantum confinement effect. Moreover, as strong experimental evidence, the phenomenon of bandgap widening displayed in Fig. 3 also proves that quantum confinement effect happened on NP-MPSi. Therefore, we infer that hydrogen termination instead of complete oxygen termination had governed the surface of NP-MPSi. In this situation, the photogenerated charge carriers (holes for N-type silicon in this work) can transfer to the surface of NP-MPSi via Si–H and then react with water or pollutants. Therefore, the photocurrent of NP-MPSi is stable even in aqueous solution.

In order to detect the surface chemical states and functional groups, MPSi and NP-MPSi samples were tested by Fourier transform infrared spectrometer (FT-IR) and X-ray photoelectron spectroscopy (XPS). The results of FT-IR were shown in Fig. 6. For MPSi before photocatalytic process, the peak for Si–H vibrations around 2300 cm^{-1} was obvious, but it disappeared after photocatalytic process, indicating that H atoms (appending on the surface of MPSi) were replaced by other atoms (it is oxygen according to the following analysis). While for NP-MPSi, the peak at around 2300 cm^{-1} was retained after photocatalytic process, meaning its Si–H bonds are relatively stable. Another difference appeared at around 950–1250 cm^{-1} which can be attributed to oxide stretching vibrations (υSiO modes) [32–34]. The oxide stretching vibrations for MPSi was very weak but after being used in photocatalytic process, the obvious peak appeared at 950–1250 cm^{-1}. This change proves that the oxidation of MPSi happened. While comparing the oxide stretching vibrations of NP-MPSi before and after photocatalytic processes, the difference of peaks at 950–1250 cm^{-1} was not noticeable. It displays the good anti-oxidation ability of NP-MPSi.

Furthermore, Fig. 7A and B demonstrate the Si 2p core level peaks for MPSi sample before and after being used in photocatalytic experiment, respectively. The peak fitting procedure was based on the use of five Gaussian-shaped peaks of Si^{n+} (n = 0, 1, 2, 3, and 4) to simulate Si, Si_2O, SiO, Si_2O_3, and SiO_2, respectively [35–37]. As shown in Fig. 7A, the peak of Si^0 was highest and the peaks corresponding to Si^{1+}, Si^{2+}, Si^{3+} and Si^{4+} can be observed, showing that the pristine Si coexists with its suboxides (including SiO_2). However, after MPSi being used in photocatalysis, the peak for Si^0 state nearly disappeared. At the same time, the peak of Si^{4+} became the highest one, revealing the oxidation process from Si to SiO_2. The XPS spectra of NP-MPSi samples were also shown in Fig. 7C and D. Comparing the XPS peaks in two figures, it can be found that peak of Si^0 was highest in both figures, and the peak intensity for Si^{4+} increased only a little. This phenomenon illuminates that little SiO_2 appeared on the surface of NP-MPSi after the photocatalytic reaction, which is consistent with FT-IR spectra.

Additionally, the ratio of surface chemical states of silicon atoms was also calculated (Fig. 8). For MPSi, the amount of Si^0 occupied the largest amount (more than 40%) before photocatalytic experiment, but it decreased to only 5% after the reaction. By contrast, the SiO_2 (Si^{4+} state) increased from 40% to more than 75%, revealing that the surface silicon atoms went through an oxidation process from

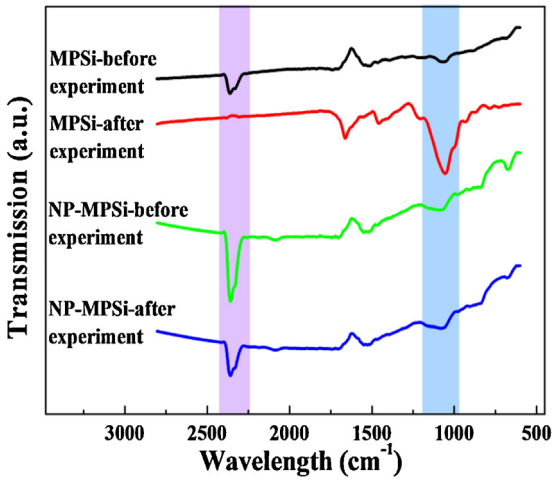

Fig. 6. FT-IR of MPSi and NP-MPSi before and after photocatalytic removal of phenol for 5 h.

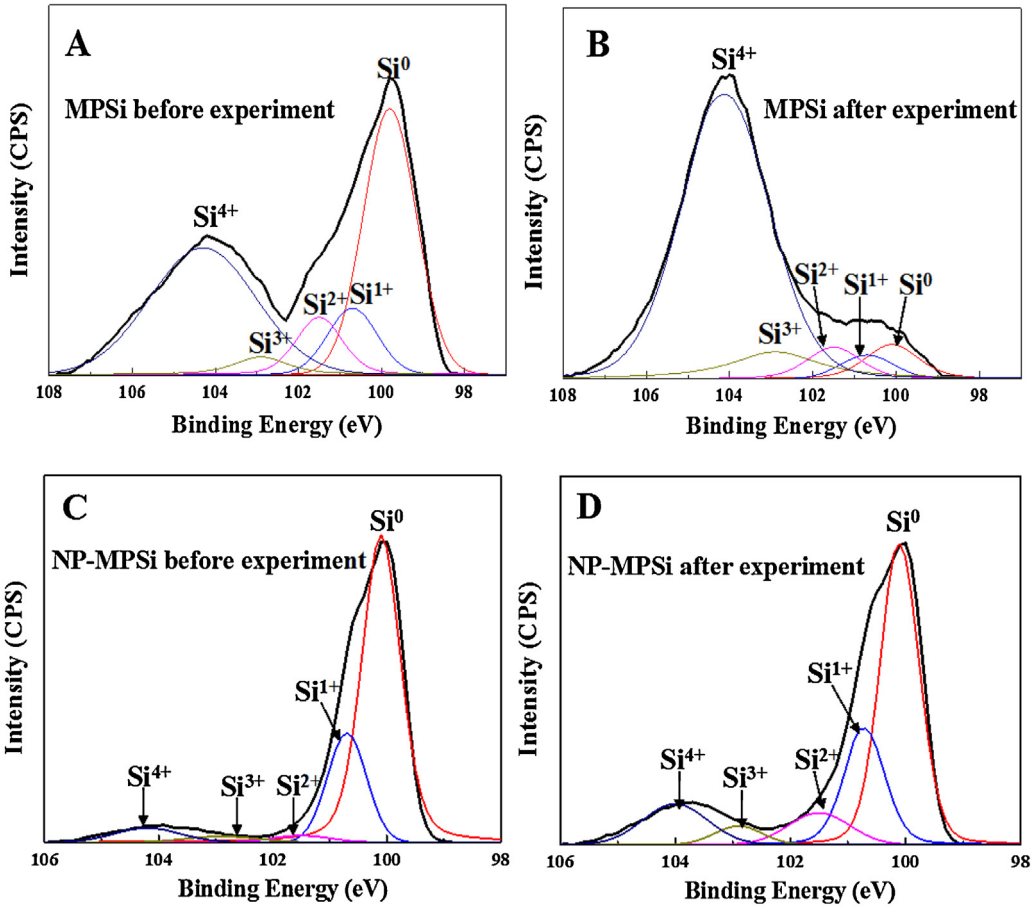

Fig. 7. Si 2p XPS spectra for MPSi (A) and (B) and NP-MPSi (C) and (D) before and after photocatalytic removal of phenol for 5 h.

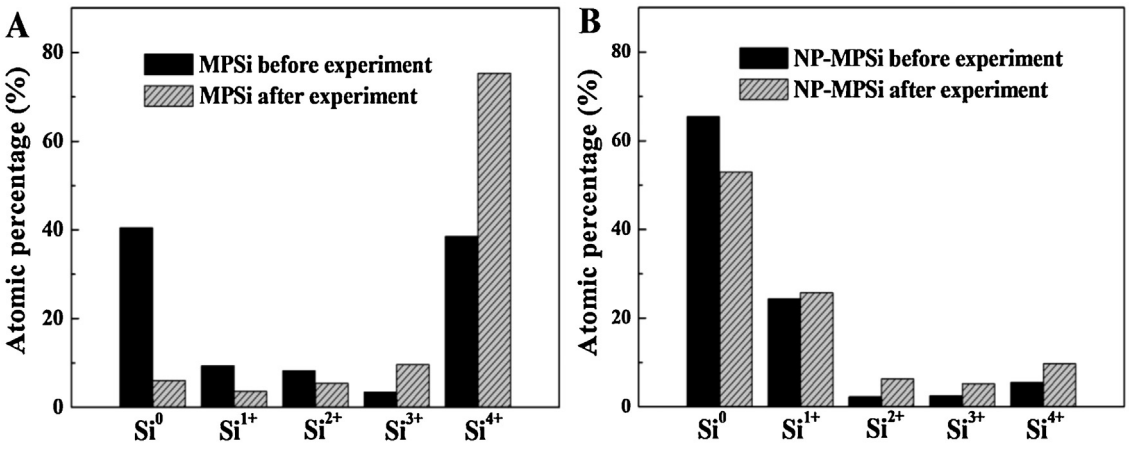

Fig. 8. Changes in the percentages of the five Si oxidation states Si^{n+} (n = 0, 1, 2, 3, and 4) for MPSi (A) and NP-MPSi (B) before and after photocatalytic removal of phenol for 5 h.

Si^0 to SiO_2. However, the Si^0 chemical state on the surface of NP-MPSi can be maintained well during the photocatalytic process, just slightly decreased from 67% before the photocatalysis to 55% after 5 h reaction (see Fig. 8B), revealing an excellent stability and enhanced photocatalytic performance in aqueous solution.

The photocatalytic stability of NP-MPSi was further investigated by recycling NP-MPSi as a photocatalyst five times. As shown in Fig. 5B, the removal efficiency of phenol remained higher than 90% even after NP-MPSi was used five times, indicating that it exhibits good photocatalytic stability in aqueous solution.

4. Conclusions

In summary, by anodic etching of a Si wafer in HF/ethanol solution (v:v = 1:1) under Xe lamp illumination, a hierarchically porous silicon structure containing uniform nanopores with a diameter less than 5 nm could be fabricated on the surface of macropores. These nanopores induce an obvious quantum confinement effect, which resulted in a larger bandgap, positive shift of the VB and hydrogen-terminated surface. Consequently, the hierarchically porous silicon material displays good stability in aqueous solution

and degrades pollutants in aqueous solution via photocatalytic oxidation even under visible light irradiation. This work is expected to open a new avenue for pure silicon photocatalyst materials in pollutant control, water splitting and other applications.

Acknowledgements

This work was supported by the National Basic Research Program of China (2011CB936002) and the National Natural Science Foundation of China (21007007).

References

[1] M. Anpo, M. Takeuch, Journal of Catalysis 216 (2003) 505–516.
[2] K.Q. Peng, S.T. Lee, Advanced Materials 23 (2011) 198–215.
[3] P.V. Kamat, Journal of Physical Chemistry C 111 (2007) 2834–2860.
[4] H.G. Kim, D.W. Hwang, J.S. Lee, Journal of the American Ceramic Society 126 (2004) 8912–8913.
[5] T. Ohnoa, M. Akiyoshi, T. Umebayashi, K. Asai, T. Mitsui, M. Matsumura, Applied Catalysis A-General 265 (2004) 115–121.
[6] Y. Cho, W. Choi, Environmental Science and Technology 35 (2001) 966–970.
[7] K. Sayama, A. Nomura, T. Arai, T. Sugita, R. Abe, M. Yanagida, T. Oi, Y. Iwasaki, Y. Abe, H. Sugihara, Journal of Physical Chemistry B 110 (2006) 11352–11360.
[8] J. Tang, Z. Zou, J. Ye, Journal of Physical Chemistry C 111 (2007) 12779–12785.
[9] F. Gao, X. Chen, K. Yin, S. Dong, Z. Ren, F. Yuan, T. Yu, Z. Zou, J.M. Liu, Advanced Materials 19 (2007) 2889–2892.
[10] B.B. Kale, J.O. Baeg, S.M. Lee, H. Chang, S.J. Moon, C.W. Lee, Advanced Functional Materials 16 (2006) 1349–1354.
[11] L. Zhang, I. Djerdj, M. Cao, M. Antonietti, M. Niederberger, Advanced Materials 19 (2007) 2083–2086.
[12] A.V. Rao1, J.N. Chazalviel, Journal of the Electrochemical Society 134 (1987) 2777–2783.
[13] K. Sakainoa, S. Adachiz, Journal of the Electrochemical Society 149 (2002) G543–G549.
[14] H. Morisaki, T. Watanabe, M. Lwase, K. Yazawa, Applied Physics Letters 29 (1976) 338–340.
[15] H. Yu, S. Chen, X. Fan, X. Quan, H. Zhao, X. Li, Y. Zhang, Angewandte Chemie International Edition 122 (2010) 1–5.
[16] N. Koshida, K. Echizenya, Journal of the Electrochemical Society 138 (1991) 837–841.
[17] M.R. Linford, C.E.D. Chidsey, Journal of the American Ceramic Society 115 (1993) 12631–12632.
[18] J. Sun, H. Lu, H. Lin, L. Du, W. Huang, H. Li, T. Cui, Separation and Purification Technology 88 (2012) 116–120.
[19] M. Shao, L. Cheng, X. Zhang, D.D.D. Ma, S. Lee, Journal of the American Ceramic Society 131 (2009) 17738–17739.
[20] N. Megouda, Y. Cofininier, S. Szunerits, T. Hadjersi, O. ElKechai, R. Boukherrou, Chemical Communications 47 (2011) 991–993.
[21] O. Fellahi, M.R. Das, Y. Coffinier, S. Szunerits, T. Hadjersi, M. Maamache, R. Boukherroub, Nanoscale 3 (2011) 4662–4669.
[22] F. Wang, Q. Yang, G. Xu, N. Lei, Y.K. Tsang, N. Wong, J.C. Ho, Nanoscale 3 (2011) 3269–3276.
[23] C. Delerue, G. Allan, M. Lannoo, Journal of Luminescence 80 (1999) 65–73.
[24] D.D.D. Ma, C.S. Lee, F.C.K. Au, S.Y. Tong, S.T. Lee, Science 299 (2003) 1874–1877.
[25] M.V. Wolkin, J. Jorne, P.M. Fauchet, G. Allan, C. Delerue, MRS Proceedings 536 (1998) 185–190.
[26] D.J. Lockwood, Z.H. Lu, J.M. Baribeau, Physical Review Letters 76 (1995) 539–541.
[27] B. Delley, E.F. Steigmeier, Physical Review B 47 (1993) 1397–1400.
[28] S.E. John, S.K. Mohapatra, M. Misra, Langmuir 25 (2009) 8240–8247.
[29] K. Prasain, T.D.T. Nguyen, M.J. Gorman, L.M. Barrigan, Z. Peng, M.R. Kanost, L.U. Syed, J. Li, K.Y. Zhu, D.H. Hua, Bioorganic and Medicinal Chemistry 20 (2012) 1679–1689.
[30] X.G. Zhang, Electrochemistry of Silicon and Its Oxide (Chinese edition), Chemical Industry Press, Beijing, 200443.
[31] W.L. Wilson, P.F. Szajowski, L.E. Brus, Science 262 (1993) 1242–1244.
[32] L. Boarino, C. Baratto, F. Geobaldo, G. Amato, E. Comini, A.M. Rossi, G. Faglia, G. Lerondel, G. Sberveglieri, Materials Science and Engineering B 69–70 (2000) 210–214.
[33] D.B. Mawhinney, J.A. Glass, J.T. Yates, Journal of Physical Chemistry B 101 (1997) 1202–1206.
[34] S. Ciampi, B. Guan, N. Darwish, P.J. Reece, J.J. Gooding, Journal of Physical Chemistry C 116 (2012) 16080–16088.
[35] Y. Liu, T.P. Chen, Y.Q. Fu, M.S. Tse, J.H. Hsieh, P.F. Ho, Y.C. Liu, Journal of Physics D: Applied Physics 36 (2003) L97–L100.
[36] W. Zhang, S. Zhang, Y. Liu, T. Chen, Journal of Crystal Growth 311 (2009) 1296–1301.
[37] B.G. Fernandez, M. Lopez, C. Garcia, A.P. Rodriguez, J.R. Morante, Journal of Applied Physics 91 (2002) 798–807.